

Topological Signatures of Heating and Dark Matter in the 21 cm Forest

Hayato Shimabukuro

*South-Western Institute for Astronomy Research (SWIFAR),
Yunnan University, Kunming, Yunnan 650500, People's Republic of China
Key Laboratory of Survey Science of Yunnan Province,
Yunnan University, Kunming, Yunnan 650500, People's Republic of China
Graduate School of Science, Division of Particle and Astrophysical Science,
Nagoya University, Chikusa-Ku, Nagoya, 464-8602, Japan**

(Dated: January 16, 2026)

We show that persistence-based topology of the 21 cm forest encodes information about Cosmic Dawn that is complementary to traditional amplitude- or correlation-based statistics. Applying topological data analysis to simulated one-dimensional forest spectra over a grid of X-ray heating efficiencies f_X and warm-dark-matter masses m_{WDM} (which set the free-streaming scale), we construct persistence diagrams and Betti-0 curves that track the birth-merger hierarchy of absorption troughs under sublevel filtrations. From these summaries we define three interpretable descriptors: the trough line density $\lambda(t_*)$, the total squared persistence $M_2 = \sum_{j \in I_{\text{long}}} \tau_j^2$, and the Betti-curve asymmetry A_{skew} . In a Fisher forecast around a fiducial WDM model, $\lambda(t_*)$ and A_{skew} provide strong local leverage on the heating axis, while M_2 retains appreciable sensitivity to the free-streaming scale and supplies an inclined constraint direction that reduces the remaining degeneracy in the (f_X, m_{WDM}) plane. We further demonstrate that, under an SKA1-Low-like uncorrelated thermal-noise model, noise predominantly produces short-lived fluctuations that are removed by a uniform persistence cut, leaving the topology of long-lived troughs and the gross Betti-curve morphology largely intact. These results establish persistence-based descriptors as a robust non-Gaussian probe of small-scale structure and heating during Cosmic Dawn, naturally complementing power-spectrum and wavelet-based analyses.

I. INTRODUCTION

The 21 cm forest consists of narrow absorption features imprinted on the spectra of high-redshift radio sources by intervening neutral hydrogen during Cosmic Dawn and the Epoch of Reionization [1–5]. These absorption structures trace the thermal and dynamical state of the intergalactic medium, linking the observed brightness temperature to the spin temperature, density fluctuations, and line-of-sight velocity gradients. As next-generation facilities such as SKA1-Low approach the sensitivity required for detecting the 21cm forest [5], identifying observables that can extract reliable physical information from its absorption morphology has become increasingly important.

A key difficulty is that astrophysical X-ray heating and dark-matter free-streaming can influence the forest in ways that look similar when viewed through traditional amplitude-based statistics. Heating raises the spin temperature toward the radiation temperature, flattening the contrast of absorption features, while dark matter with a finite free-streaming scale suppresses small-scale density fluctuations and reduces the number of absorption minima. When characterized using the one-dimensional power spectrum or related amplitude-weighted measures, these two mechanisms often lead to comparable reductions of small-scale power [6–17].

Higher-order or multiscale statistics, including wavelet scattering transforms [18–22], extend sensitivity to non-linear structure but remain fundamentally tied to fluctuation amplitudes. Recent AI/ML-based approaches have also demonstrated the ability to extract non-Gaussian information from 21 cm observables beyond correlation-based statistics [23, 24]. These methods are promising, but their performance typically depends on the training domain and on how observational systematics and foreground or calibration residuals are represented in the training data. This motivates complementary summary statistics that are physically interpretable, can be stress-tested under controlled forward models, and target aspects of the absorption morphology not reducible to amplitudes alone.

From a physical standpoint, the two processes also differ in how they reshape absorption morphology: dark-matter free streaming eliminates shallow extrema and changes how neighboring troughs merge, whereas X-ray heating largely produces a monotonic remapping of the brightness-temperature field that tends to preserve the rank ordering of local minima. This suggests that summaries sensitive to the organization and merging hierarchy of troughs, rather than amplitudes alone, are natural candidates for separating heating from free streaming.

Topological data analysis (TDA) provides a principled framework for extracting this type of information [25–27]. In a one-dimensional field, sublevel filtrations track the emergence and merger of connected components as the threshold value rises from deep to shallow intensities. Persistence diagrams and Betti curves summarize these events by encoding the hierarchy of absorption troughs in

*Electronic address: shimabukuro@ynu.edu.cn

terms of their birth values, lifetimes, and merger structure. These topological summaries capture the organization of minima and are invariant under smooth monotonic transformations of the field, a property that aligns closely with the qualitative effect of X-ray heating, while remaining sensitive to the removal of small-scale structure induced by dark-matter free streaming.

Topological approaches have already proven valuable in various cosmological contexts, including studies of the cosmic web, reionization morphology, and weak-lensing convergence fields [28–34]. However, the absorption topology of the 21 cm forest has not yet been explored. The forest is particularly well suited for such an analysis because its one-dimensional nature allows the full merger hierarchy of absorption features to be characterized without ambiguity, and because the narrow spectral structures expected during Cosmic Dawn are well resolved at kilohertz-level channel widths available to SKA1-Low.

In this work we introduce a topological framework for analyzing the 21 cm forest and examine its potential to separate the physical effects of X-ray heating and dark-matter free streaming. By focusing on the connectivity and rank structure of absorption troughs rather than on their amplitudes alone, topology offers a complementary perspective on the forest that is naturally robust to monotonic distortions and, in practice, can mitigate certain calibration and continuum residuals after appropriate preprocessing. This conceptual foundation provides a basis for incorporating topological information into future studies of the 21 cm forest and for enhancing the physical insights that upcoming observations may deliver.

II. FORMALISM OF THE 21CM FOREST

We analyze mock one-dimensional 21 cm forest spectra generated from the semi-numerical simulations of Shao et al. [19], which model the intergalactic medium (IGM) during Cosmic Dawn and the Epoch of Reionization for both cold and warm dark-matter cosmologies. These simulations incorporate radiative and X-ray heating processes with varying efficiencies and produce self-consistent density, spin-temperature, and ionization fields. In the following analysis, the thermal history of the IGM is controlled by the X-ray heating efficiency parameter f_X , which rescales the X-ray emissivity of early sources relative to a fiducial model, with larger values corresponding to more efficient heating. The nature of dark matter is parameterized by the warm-dark-matter particle mass m_{WDM} , which sets the free-streaming scale and determines the degree of suppression of small-scale density fluctuations; the limit $m_{\text{WDM}} \rightarrow \infty$ corresponds to the standard cold dark matter (CDM) scenario.

Figure 1 shows representative noise-free 21 cm forest spectra from these simulations. The spectra consist of narrow absorption troughs imprinted by intervening neutral hydrogen along the line of sight, whose depth, abun-

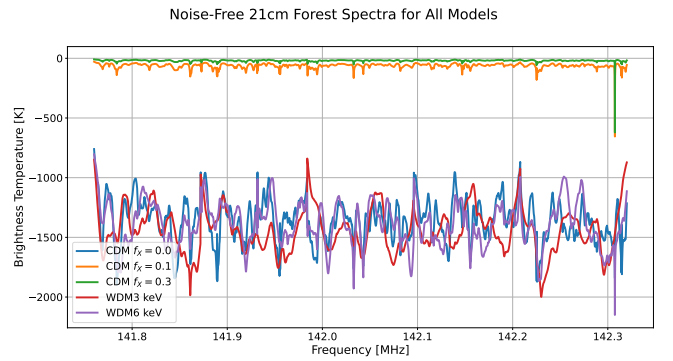


FIG. 1: Representative noise-free one-dimensional 21 cm forest spectra in term of brightness temperature at $z \simeq 9$ for the models explored in this work: CDM with varying X-ray heating efficiency ($f_X = 0, 0.1, 0.3$) and WDM models with $m_{\text{WDM}} = 3, 6$ keV (at $f_X = 0$). Narrow absorption troughs trace intervening neutral hydrogen and encode both the thermal state (heating) and the suppression of small-scale structure (free streaming).

dance, and apparent merging behavior vary with the thermal and small-scale structure of the IGM. The figure is included to provide a visual illustration of the one-dimensional absorption morphology and is not used as a quantitative result in this work.

The observable differential brightness temperature relative to the cosmic microwave background (CMB) is

$$\delta T_b(\nu) \simeq 27 x_{\text{HI}}(1 + \delta) \left(1 - \frac{T_{\text{CMB}}}{T_S}\right) \left(\frac{1+z}{10} \frac{0.15}{\Omega_m h^2}\right)^{1/2} \times \left(\frac{\Omega_b h^2}{0.023}\right) \text{ mK}, \quad (1)$$

where x_{HI} is the neutral hydrogen fraction, δ is the baryonic overdensity, and T_S is the hydrogen spin temperature. Here $T_{\text{CMB}} = 2.725(1+z)$ K denotes the CMB temperature at redshift z , Ω_m and Ω_b are the present-day matter and baryon density parameters, and h is the dimensionless Hubble parameter defined by $H_0 = 100 h \text{ km s}^{-1} \text{ Mpc}^{-1}$. The observing frequency ν is related to redshift by $\nu = \nu_{21}/(1+z)$, where $\nu_{21} = 1420.40575$ MHz is the rest-frame frequency of the 21 cm hyperfine transition. Equation (1) shows that the absorption strength depends on both the thermal state of the gas, through T_S , and the small-scale density structure of the IGM, through δ and x_{HI} .

The corresponding 21 cm optical depth along each line of sight is computed as

$$\tau_\nu = \frac{3h_P c^3 A_{10} n_{\text{HI}}}{16k_B T_S \nu_{21}^2 H(z)} \times \left(1 + \frac{1}{H(z)} \frac{dv_{\parallel}}{dr_{\parallel}}\right)^{-1}, \quad (2)$$

where h_P is Planck's constant, c is the speed of light, k_B is Boltzmann's constant, and A_{10} is the spontaneous

Einstein coefficient of the 21 cm transition. The quantity n_{HI} denotes the neutral hydrogen number density, $H(z)$ is the Hubble expansion rate at redshift z , and $dv_{\parallel}/dr_{\parallel}$ is the line-of-sight peculiar-velocity gradient along the co-moving coordinate r_{\parallel} . The optical depth maps directly to the transmitted flux, $F = e^{-\tau_{\nu}}$. Variations in T_S , n_{HI} , and the velocity field imprint narrow absorption features whose morphology carries information about local density structure and heating.

For each model we analyze ten independent realizations, each providing ten lines of sight spanning 10 cMpc, sampled at 1 kHz, matching the expected channel width of SKA1-Low [35]. The choice of ten sightlines is motivated by theoretical estimates suggesting that approximately twenty bright radio quasars may exist at $z \simeq 9$ [36], implying that our sample size is representative of realistic observational prospects.

Before applying the topological analysis, each raw spectrum $x(\nu)$ is detrended and standardized. We adopt a Z-score normalization,

$$Z(\nu) = \frac{x(\nu) - \langle x \rangle}{\sigma_x}, \quad (3)$$

where $\langle x \rangle$ and σ_x denote the mean and standard deviation along the same line of sight. This standardization removes differences in overall amplitude and rescales all models onto a common threshold axis, ensuring that the subsequent analysis is sensitive to morphological structure rather than absolute-amplitude variations.

III. TOPOLOGICAL FORMALISM

In a one-dimensional field such as $Z(\nu)$, topological information can be extracted by tracking how absorption troughs appear, persist, and merge as an intensity threshold t is swept across the brightness-temperature landscape. Concretely, for each t we consider the connected regions where the field lies below the threshold, and follow how the connectivity of these regions evolves as t is raised from deep to shallow values. This threshold-sweep view provides a natural description of the birth-merger hierarchy of absorption features.

Because this construction is driven by the order in which extrema and saddle-like merge events are encountered during the sweep, it depends primarily on the relative depth hierarchy among pixels rather than on their absolute amplitudes. We refer to this property as rank ordering: only the ordering of values from deeper to shallower matters, not the exact numerical separations between them. A smooth monotonic remapping of the field, such as that induced by X-ray heating, preserves the rank ordering and therefore leaves the underlying connectivity evolution essentially unchanged (up to a reparameterization of the threshold axis). In contrast, dark-matter free streaming can erase or merge shallow extrema, thereby altering the set of minima and their merger hierarchy.

Strictly speaking, the topology defined by this threshold-based construction is invariant under smooth monotonic remappings of the field, provided thresholds are reparameterized accordingly. In the language of topology, this is the invariance of the sublevel-set filtration. In practice, however, our summary descriptors are evaluated with a common persistence cut τ_{\star} and with a reference threshold defined for each line of sight (e.g., the peak of the persistence-filtered Betti-0 curve). Under these conventions, even a monotonic remapping can shift the Betti support along the threshold axis and thereby modify shape-based descriptors, while changes that erase or merge extrema (such as free streaming) alter the merger hierarchy itself.

A. Sublevel filtrations and persistence

For a one-dimensional field $Z(\nu)$, the sublevel set at threshold t is

$$X_t = \{ \nu \mid Z(\nu) \leq t \}. \quad (4)$$

As the threshold is raised from deep to shallow values, new absorption troughs appear as isolated connected components and later merge with deeper structures. This procedure defines a filtration $\{X_t\}_{t \in \mathbb{R}}$, and the evolution of connected components is encoded in the zeroth homology group $H_0(X_t)$.

Each connected component has a birth threshold b_j at which it appears, and a death threshold d_j at which it merges with an older (deeper) component. The collection of points (b_j, d_j) forms the persistence diagram (PD), and the persistence lifetime

$$\tau_j = d_j - b_j \quad (5)$$

quantifies the prominence of an absorption trough. Hereafter, τ denotes the persistence lifetime, not the optical depth. Long-lived features correspond to deep, well-separated troughs, while short-lived features track shallow fluctuations that are easily erased by noise or small-scale smoothing. Figure 2 provides a schematic illustration of this construction for a one-dimensional field, showing how absorption troughs are born and merge under a threshold sweep and how these events are mapped onto the persistence diagram.

A complementary summary is the Betti-0 curve,

$$\beta_0(t) = \#\{j \mid b_j \leq t < d_j\}, \quad (6)$$

which counts the number of connected absorption components alive at threshold t . Betti-0 therefore traces how many distinct troughs remain separated at a given depth and provides a direct measure of the merger hierarchy of potential wells in the IGM.

Having defined the Betti-0 curve, it is useful to clarify its relation to Minkowski functionals, which are widely used to quantify morphology in cosmology. Both approaches start from thresholded excursion sets: given a

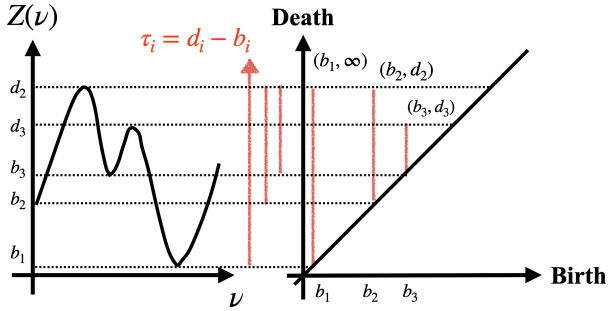


FIG. 2: Schematic illustration of the sublevel-set filtration and the corresponding persistence diagram for a one-dimensional field $Z(\nu)$. Connected components are born at local minima (b_i) and merge at higher thresholds (d_i), yielding persistence pairs (b_i, d_i) with lifetime $\tau_i = d_i - b_i$. The most persistent component does not merge within the filtration range.

threshold t , one studies the geometry and connectivity of the set $X_t = \{\nu | Z(\nu) \leq t\}$ (or, equivalently, superlevel sets). In one dimension, the Minkowski description reduces essentially to the measure (total length) of X_t and its Euler characteristic $\chi(X_t)$. Because one-dimensional excursion sets have no loops, $\chi(X_t)$ is equal to the number of connected components, and therefore coincides with the Betti-0 number, $\chi(X_t) = \beta_0(t)$. In this sense, the Betti-0 curve can be viewed as the connectivity part of the Minkowski description evaluated as a function of threshold. The persistence diagram extends this picture by recording when each connected component is created and when it merges as the threshold varies, thereby encoding the full merger hierarchy of troughs across thresholds rather than a snapshot at each t .

Figure 3 illustrates this construction schematically for a one-dimensional absorption field. As the threshold t is increased from deep to shallow values, new connected components are created at local minima of $Z(\nu)$, while existing components merge when the threshold reaches higher saddle points. The Betti-0 number $\beta_0(t)$ therefore counts the number of connected components in the sublevel set X_t at each threshold, encoding the birth-merger hierarchy of absorption troughs along the line of sight.

B. Persistence filtering and reference thresholds

The raw PD contains many short-lived features associated with shallow or noise-like fluctuations. To isolate physically meaningful troughs, we impose a persistence cut

$$\tau_* = 0.411, \quad (7)$$

chosen as the 95th percentile of the baseline (noiseless CDM) model. This defines the set of long-lived compo-

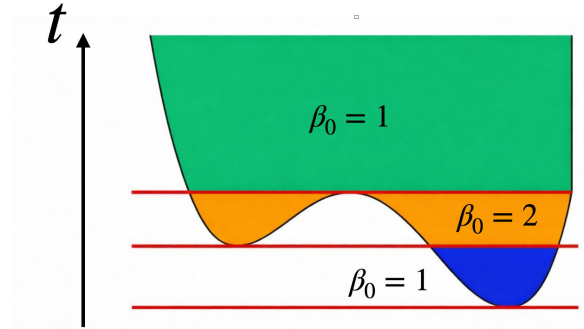


FIG. 3: Schematic illustration of a sublevel-set filtration for a one-dimensional absorption field. As the threshold t is increased (from deeper to shallower absorption levels), disconnected absorption troughs appear and subsequently merge. The Betti-0 number $\beta_0(t)$ counts the number of connected components at each threshold and changes discretely when merger events occur. This figure is purely illustrative and is intended to clarify the definition of $\beta_0(t)$.

nents

$$\mathcal{I}_{\text{long}} = \{j : \tau_j \geq \tau_*\}. \quad (8)$$

The precise value of τ_* is not essential; varying it within reasonable bounds preserves all qualitative trends. Unless stated otherwise, whenever a descriptor requires an intensity threshold we define a line-of-sight-dependent reference value $t_{*,\ell} \equiv \arg \max_t \beta_{0,\ell}(t)$ from the persistence-filtered Betti-0 curve of that LOS, and we report LOS-averaged descriptor values. For notational simplicity, we often omit the LOS index and write t_* . This peak-based convention avoids imposing an external absolute threshold but implies that model-dependent shifts of the Betti support along the threshold axis can contribute to the response of λ and A_{skew} in addition to changes in the underlying merger hierarchy.

C. Topological descriptors

From the PD we construct three physically interpretable descriptors that capture complementary aspects of the absorption morphology. Together, these quantities summarize how many independent troughs exist, how broadly their lifetimes are distributed, and whether the lifetime distribution is dominated by long- or short-lived components. These descriptors respond in distinct ways to heating and dark-matter free-streaming, thereby helping to break their degeneracy. Rather than working directly with the full persistence diagram, we compress its information into a small set of summary descriptors that are robust, physically interpretable, and amenable to statistical inference.

a. (i) Trough line density. For a frequency span $\Delta\nu$ at redshift z , the corresponding comoving line-of-sight

length is

$$L_{\parallel} = \Delta\nu \frac{d\chi}{d\nu}, \quad \frac{d\chi}{d\nu} = \frac{c(1+z)^2}{H(z)\nu_{21}}. \quad (9)$$

The line density of absorption troughs is then

$$\lambda(t_{\star}) = \frac{\beta_0(t_{\star})}{L_{\parallel}} \text{ [Mpc}^{-1}\text{]}, \quad (10)$$

which measures the abundance of distinct troughs at the fiducial threshold. Warm dark matter suppresses small-scale structure and therefore reduces λ , while X-ray heating also decreases λ by homogenizing the temperature field.

b. (ii) Total squared persistence. To capture the "strength" of the absorption features, we compute the sum of the squared lifetimes for all long-lived components ($\tau_j \geq \tau_{\star}$). We define the second moment sum as

$$M_2 = \sum_{j \in \mathcal{I}_{\text{long}}} \tau_j^2. \quad (11)$$

Unlike a simple count, M_2 weights features by their prominence (lifetime). Since X-ray heating compresses the contrast of absorption troughs (reducing τ_j), M_2 decreases rapidly with increasing f_X , making it a sensitive probe of the thermal state of the IGM. At the same time, warm dark matter suppresses small-scale extrema and shortens the overall lifetime distribution, leading to a systematic reduction of M_2 even in the absence of strong heating.

c. (iii) Betti curve asymmetry. Finally, we characterize the shape of the brightness-temperature distribution by quantifying the asymmetry of the Betti-0 curve $\beta_0(t)$. The support of $\beta_0(t)$ reflects the depth range of absorption features. Let t_p be the threshold value corresponding to the p -th percentile of the cumulative area under the $\beta_0(t)$ curve, defined such that $\int_{-\infty}^{t_p} \beta_0(t') dt' = \frac{p}{100} \int_{-\infty}^{\infty} \beta_0(t') dt'$. Using the peak position t_{\star} as a reference, we define the asymmetry factor A_{skew} as the ratio of the widths of the shallow (right) and deep (left) sides of the distribution:

$$A_{\text{skew}} = \frac{t_{95} - t_{\star}}{t_{\star} - t_{05}}. \quad (12)$$

Here, t_{95} characterizes the boundary of shallow fluctuations, while t_{05} marks the deep absorption tail. The use of percentile-based widths ensures that A_{skew} is insensitive to the absolute normalization of $\beta_0(t)$ and robust against isolated outliers in the distribution.

X-ray heating acts, to leading order, as a monotonic remapping of the field intensity, which can distort the shape of $\beta_0(t)$ and alter the balance between the deep and shallow wings. In contrast, warm dark matter primarily suppresses the abundance of features while preserving the relative shape of the surviving distribution more effectively. This difference renders A_{skew} primarily sensitive to f_X (orthogonal to λ).

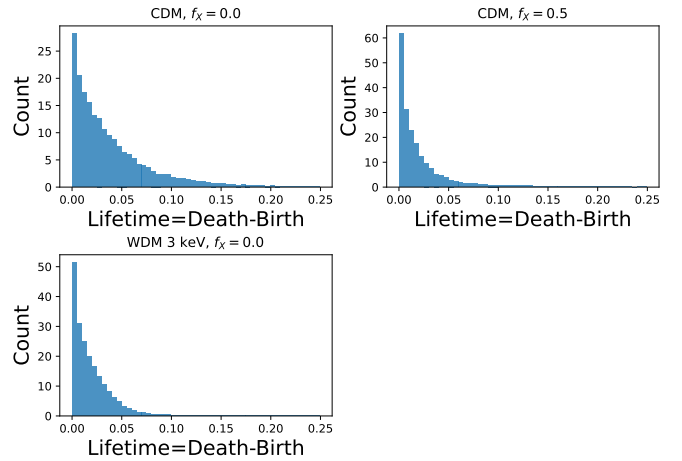


FIG. 4: **Distributions of persistence lifetimes(Death-Birth)** Panels compare CDM with $f_X = 0$ and 0.5 and CDM ($f_X = 0$) versus WDM ($m_{\text{WDM}} = 3 \text{ keV}$, $f_X = 0$).

IV. RESULTS

A. Persistence lifetime distributions

Figure 4 compares the distributions of persistence lifetimes $\tau = d - b$ using common bins across models. For CDM, increasing f_X redistributes probability toward shorter lifetimes and suppresses the long- τ tail, consistent with reduced trough contrast under stronger X-ray heating. For WDM ($m_{\text{WDM}} = 3 \text{ keV}$, $f_X = 0$), the distribution is likewise shifted toward shorter lifetimes and shows a depleted long- τ tail, reflecting the suppression of small-scale extrema and earlier merging of neighboring troughs. These changes imply that tail-sensitive summaries, such as the mass above a fixed lifetime cut and the resulting number of long-lived components N_{long} , should decrease as the long- τ tail is trimmed; we quantify this behavior explicitly in the topological descriptors introduced below.

B. Betti-0 curves

Figure 5 presents the Betti-0 curves, i.e., the number of connected components $\beta_0(t)$ alive at threshold t , for standardized brightness-temperature spectra at a spectral resolution of 1 kHz. We focus first on the persistence-filtered curves (bottom panel), which isolate the topologically significant absorption troughs.

With persistence filtering applied, $\beta_0(t)$ exhibits a single pronounced peak as a function of t . The rise toward the peak reflects the appearance of distinct troughs as the threshold enters the typical absorption depths, whereas the decline beyond the peak reflects the progressive merging of neighboring troughs as the threshold is increased. The peak height therefore encodes the abundance of independent absorption features, while the peak width characterizes the range of thresholds over which these features

remain distinct.

For the unheated CDM case ($f_X = 0$), $\beta_0(t)$ shows a high and broad peak, indicating many absorption troughs that remain separate over a wide threshold range. Increasing the X-ray heating efficiency reduces and narrows the peak, consistent with contrast compression and a more homogeneous absorption landscape. The WDM model ($m_{\text{WDM}} = 3 \text{ keV}$, $f_X = 0$) yields an even smaller and sharper peak, consistent with the suppression of small-scale extrema and the earlier merging of surviving troughs. Notably, this relative ordering differs from what is often emphasized by amplitude-based summaries. Many amplitude-based statistics respond most strongly to X-ray heating because heating raises the spin temperature and compresses the overall absorption contrast, thereby reducing the fluctuation amplitude in a largely global manner. In contrast, warm-dark-matter free streaming primarily suppresses small-scale density extrema and changes the merger hierarchy of neighboring troughs, which can have a comparatively smaller imprint on purely amplitude-based measures while leaving a clear signature in connectivity-based statistics. The Betti-0 response therefore highlights the impact of free streaming on the connectivity evolution, illustrating the complementary information captured by topology.

To clarify the role of persistence filtering, the top panel shows the unfiltered Betti-0 curves. Without filtering, the raw curves include numerous short-lived components associated with weak fluctuations and noise-like features, which introduce small oscillations and artificially broaden the $\beta_0(t)$ profiles, partially obscuring the underlying cosmological trends. We therefore apply a uniform persistence threshold $\tau \geq 0.411$, chosen as the 95 % of the lifetime distribution in the baseline noiseless CDM model, to remove low-persistence features while retaining long-lived absorption troughs that reflect the IGM morphology.

Overall, the comparison between unfiltered and filtered analyses demonstrates that persistence filtering isolates the robust topological backbone of the 21 cm forest. The adopted 1 kHz resolution ensures that the narrow absorption features expected in SKA1-Low observations are sufficiently resolved to capture their intrinsic topological structure.

C. Impact of observational effects

We investigate how spectral resolution and thermal noise affect the topology of the 21 cm forest in the fiducial CDM model with $f_X = 0$, as summarized in Figure 6. We apply the same analysis pipeline to all spectra, consisting of detrending, per-LOS standardization, downsampling, sublevel filtration, and Betti-0 evaluation, using a fixed persistence threshold $\tau \geq 0.411$. The left panel shows the dependence on spectral resolution in the absence of thermal noise by varying the channel width $\Delta\nu$. Because the descriptors are evaluated after applying a common lifetime cut, the persistence-filtered Betti-0 response need

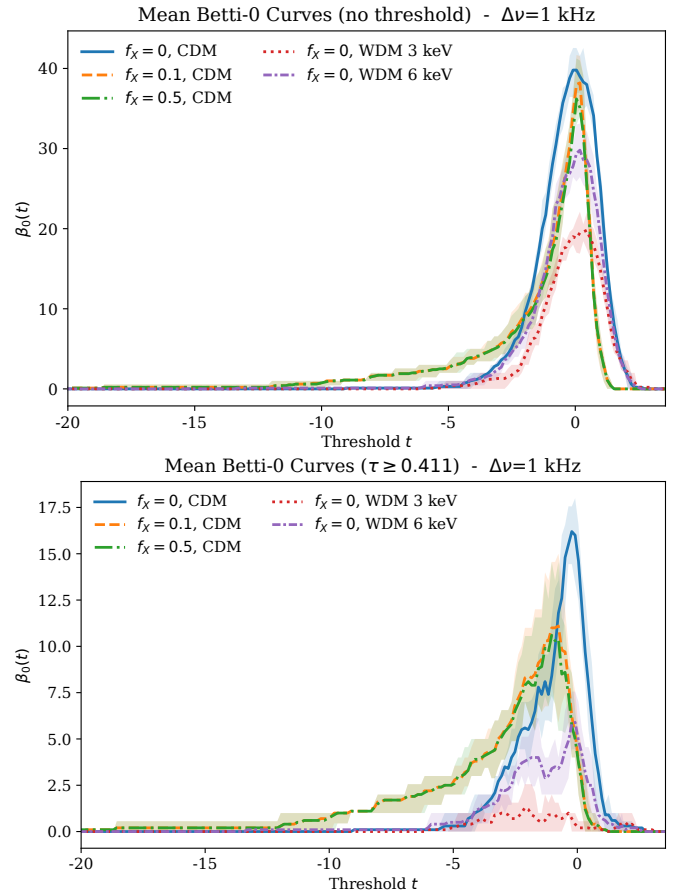


FIG. 5: Mean Betti-0 curves $\langle\beta_0(t)\rangle$ at $\Delta\nu = 1 \text{ kHz}$. Top: without persistence filtering. Bottom: after applying a uniform persistence cut $\tau \geq 0.411$, which suppresses short-lived features and clarifies model differences. Shaded regions show the central 68% interval across lines of sight.

not vary monotonically with $\Delta\nu$: spectral averaging can suppress short-lived fluctuations while simultaneously increasing the typical lifetimes of the surviving troughs, thereby changing how many components pass the fixed persistence threshold.

To model instrumental thermal noise, we adopt the radiometer equation and add Gaussian noise independent in each frequency channel. The rms noise in flux density is

$$\sigma_S(\nu) = \frac{\text{SEFD}(\nu)}{\sqrt{n_{\text{pol}} t_{\text{int}} \Delta\nu}}, \quad (13)$$

where $\text{SEFD}(\nu) = 2k_{\text{B}}T_{\text{sys}}(\nu)/A_{\text{eff}}(\nu)$, $n_{\text{pol}} = 2$ is the number of polarizations, t_{int} is the integration time per background source, and $\Delta\nu$ is the channel width. In a fully self-consistent observing model, the thermal-noise level decreases with increasing channel width as $\sigma_S \propto (\Delta\nu)^{-1/2}$; in Figure 6 we intentionally decouple this dependence by holding the noise model fixed when varying $\Delta\nu$ (left panel) to isolate the morphological effect of spectral averaging.

We convert the flux-density noise $\sigma_S(\nu)$ into the corresponding relative noise level in the absorbed spectrum by normalizing to the background-source continuum, $\sigma_{\text{rel}}(\nu) = \sigma_S(\nu)/S_\nu$. A Gaussian random realization with variance $\sigma_{\text{rel}}^2(\nu)$ is added prior to applying the same detrending and per-LOS standardization used throughout. We adopt a fiducial continuum level S_ν (and spectral shape) for the background radio source, so the quoted noise levels are conditional on this choice; results for other sources can be rescaled as $\sigma_{\text{rel}} \propto 1/S_\nu$.

The right panel then illustrates the impact of thermal noise at fixed $\Delta\nu = 1$ kHz, showing a noiseless reference case and thermal-noise realizations corresponding to $t_{\text{int}} = 100$ and 1000 h per background source under SKA1-Low-like conditions [35]. Thermal noise introduces numerous short-lived, shallow fluctuations that can artificially increase $\beta_0(t)$ at high thresholds, but applying the same persistence cut efficiently suppresses these spurious components and isolates long-lived absorption structures. As t_{int} increases, the Betti-0 curve converges toward the noiseless case and the line-of-sight scatter decreases, demonstrating that the intrinsic topological signal remains detectable under realistic SKA-like noise levels.

D. Topological degeneracy maps

Figure 7 summarizes the global trends of the three descriptors using signed Z -difference maps relative to the baseline (CDM, $f_X = 0$). For each model we compute the LOS-averaged descriptor value μ and an associated LOS scatter estimated from the 16–84 percentile range, and form a signed effect-size relative to the baseline. All descriptors use the same persistence cut τ_* , while quantities involving the threshold are evaluated at a line-of-sight-dependent reference level $t_{*,\ell} \equiv \arg \max_t \beta_{0,\ell}(t)$ obtained from the persistence-filtered Betti-0 curve. Consequently, the sign of the Z -difference reflects not only changes in the abundance and lifetimes of robust troughs, but also model-dependent shifts in the placement and shape of $\beta_0(t)$ that move the peak position across LOS.

The trough line density $\lambda(t_{*,\ell}) = \beta_{0,\ell}(t_{*,\ell})/L_{\parallel}$ measures the number density of connected components at the characteristic threshold where each LOS attains maximal connectivity. In the noiseless case, decreasing m_{WDM} suppresses small-scale extrema and typically lowers the peak height of $\beta_0(t)$, leading to smaller λ than in the baseline model. With thermal noise, many short-lived fluctuations are removed by the persistence cut, and the remaining Betti support and its peak position can shift across LOS; this can weaken the apparent dependence of λ on m_{WDM} and enhance the relative role of f_X through changes in the Betti-curve morphology.

The total squared persistence $M_2 = \sum_{j \in \mathcal{I}_{\text{long}}} \tau_j^2$ captures the cumulative prominence of long-lived troughs selected by the uniform lifetime cut. Increasing f_X tends to shorten lifetimes by compressing contrast, while free

streaming reduces the abundance of small-scale absorbers and reshapes the lifetime distribution. Accordingly, M_2 responds to both parameters and provides a sensitivity direction complementary to those of λ and A_{skew} .

The Betti-curve asymmetry A_{skew} quantifies whether the support of $\beta_0(t)$ is weighted toward deep or shallow thresholds. Because it depends on the relative placement of the Betti support along the threshold axis, A_{skew} is particularly sensitive to heating-driven remappings that distort the balance between the deep and shallow wings, providing information distinct from the primarily count-based λ and the lifetime-weighted M_2 .

Thermal noise generates many low-persistence fluctuations, but these are efficiently suppressed by the uniform lifetime threshold. The residual large-scale gradients in Fig. 7 therefore, trace robust, long-lived absorption structures and the shape of their Betti support, providing a compact visualization of how heating and free streaming imprint complementary signatures in the descriptor space.

E. Fisher forecast from topological metrics with SKA1-Low noise

To quantify how well the topological descriptors can jointly constrain X-ray heating and warm dark matter in a realistic experiment, we perform a two-parameter Fisher-matrix forecast based on the metrics introduced above. We take the parameter vector $\theta = (f_X, m_{\text{WDM}})$, where f_X rescales the X-ray emissivity and m_{WDM} is the thermal relic mass of the warm dark matter model. For each point on the simulation grid in (f_X, m_{WDM}) , we analyze 10 independent realizations, each providing 10 lines of sight (LOS). The three summary statistics $\mu = \{\lambda(t_*), M_2, A_{\text{skew}}\}$ are first averaged over the 10 LOS within each realization, and the realization-to-realization scatter σ_α is estimated from the dispersion across the 10 realizations. The spectra used here include SKA1-Low-like thermal noise corresponding to an integration time of 1000 h per background source.

Assuming N_{los} independent background radio sources, we approximate the covariance of the measured metrics as diagonal,

$$C_{\alpha\beta} = \delta_{\alpha\beta} \frac{\sigma_\alpha^2}{N_{\text{los}}}, \quad (14)$$

and neglect correlations between different metrics. In principle, the three summaries are derived from the same persistence information and may therefore exhibit non-zero cross-correlations; however, in this work we do not attempt to estimate a full covariance matrix from our finite ensemble, and we adopt the diagonal approximation as a simplifying assumption to illustrate the relative constraining power and degeneracy directions. The Fisher matrix is then

$$F_{ij} = \sum_{\alpha,\beta} \frac{\partial \mu_\alpha}{\partial \theta_i} (C^{-1})_{\alpha\beta} \frac{\partial \mu_\beta}{\partial \theta_j}, \quad (15)$$

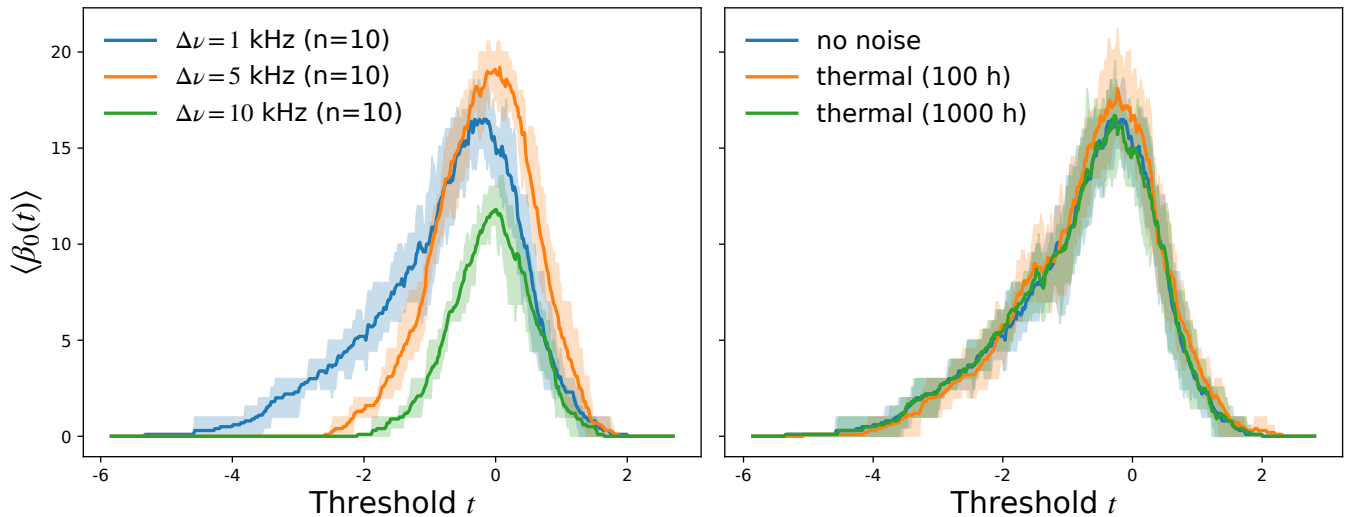


FIG. 6: **Topological sensitivity for CDM** ($f_X = 0$). A common persistence cut $\tau \geq 0.411$ is used. **Left:** Resolution dependence (1, 5, 10 kHz) shown without thermal noise. **Right:** Thermal noise at 1 kHz (noiseless, $t_{\text{int}} = 100$ and 1000 h): increasing t_{int} lowers the noise level, reduces LOS scatter, and brings the mean $\beta_0(t)$ closer to the noiseless case.

evaluated at a fiducial model θ_{fid} . Throughout this section we adopt as fiducial model a moderately heated WDM scenario with $m_{\text{WDM}} = 4$ keV and $f_X = 0.2$.

Before presenting the Fisher ellipse, it is instructive to visualize the local parameter response of each descriptor using one-dimensional slices through the fiducial point. Figure 8 shows $\lambda(t_*)$, M_2 , and A_{skew} as functions of f_X at fixed $m_{\text{WDM}} = 4$ keV (top row) and as functions of m_{WDM} at fixed $f_X = 0.2$ (bottom row), including the realization-level scatter. In the vicinity of the fiducial point, $\lambda(t_*)$ and A_{skew} exhibit a clearly stronger dependence on f_X than on m_{WDM} over our sampled grid. At the same time, M_2 retains sensitivity to both parameters and shows a comparatively clearer trend with m_{WDM} in the fiducial neighborhood. This separation of local response directions anticipates the complementarity seen in the Fisher constraints.

Figure 9 shows the resulting 1σ confidence region in the (f_X, m_{WDM}) plane. The black ellipse corresponds to the combined Fisher matrix using all three statistics, $\{\lambda(t_*), M_2, A_{\text{skew}}\}$, while the colored curves indicate the constraints obtained when each metric is used in isolation (some are truncated by the plotting window).

The orientation of each ellipse follows directly from the local gradients of the corresponding metric. In a two-parameter Fisher forecast, the long axis of an individual-metric ellipse points along the direction in parameter space to which that metric is least sensitive: moving along this axis produces comparatively little change in the metric and therefore yields weaker constraints. Conversely, the short axis aligns with the direction of maximal local sensitivity.

Consistent with Fig. 8, the $\lambda(t_*)$ constraint is highly elongated with a degeneracy direction close to vertical in this fiducial region. This reflects the fact that, once

thermal noise and persistence filtering are included, $\lambda(t_*)$ varies more strongly with f_X than with m_{WDM} near θ_{fid} . Physically, in our noise-realistic setting the component count evaluated at the reference threshold is governed primarily by heating-induced remapping and contrast compression around t_* , while the residual dependence on free streaming is subdominant at the fiducial point.

The M_2 constraint is tilted with an intermediate degeneracy direction. Since M_2 weights long-lived troughs by τ^2 , it responds both to heating, which compresses contrast and shortens persistence, and to warm-dark-matter free streaming, which modifies the abundance and lifetimes of small-scale absorbers. This mixed sensitivity yields a diagonal response in (f_X, m_{WDM}) and provides leverage complementary to $\lambda(t_*)$ and A_{skew} .

Finally, A_{skew} shows a sensitivity direction that differs from both $\lambda(t_*)$ and M_2 . Because A_{skew} is controlled by the relative support of $\beta_0(t)$ on the deep and shallow sides, it is especially responsive to heating-driven shifts of the Betti support along the threshold axis. Over the parameter range sampled here, its dependence on m_{WDM} remains comparatively weaker, producing an elongation direction that is approximately complementary to that of M_2 in the fiducial neighborhood.

Taken together, the three descriptors probe distinct combinations of f_X and m_{WDM} under realistic SKA1-Low noise. The joint 1σ ellipse is therefore substantially smaller than the broad degeneracy regions from any single metric: $\lambda(t_*)$ and A_{skew} primarily restrict the heating direction in the fiducial region, while M_2 supplies additional leverage along a mixed heating and free-streaming direction and reduces the remaining allowed parameter volume. Although simplified, this forecast demonstrates that topological summaries of the 21 cm forest remain informative for joint inference of heating and warm-dark-

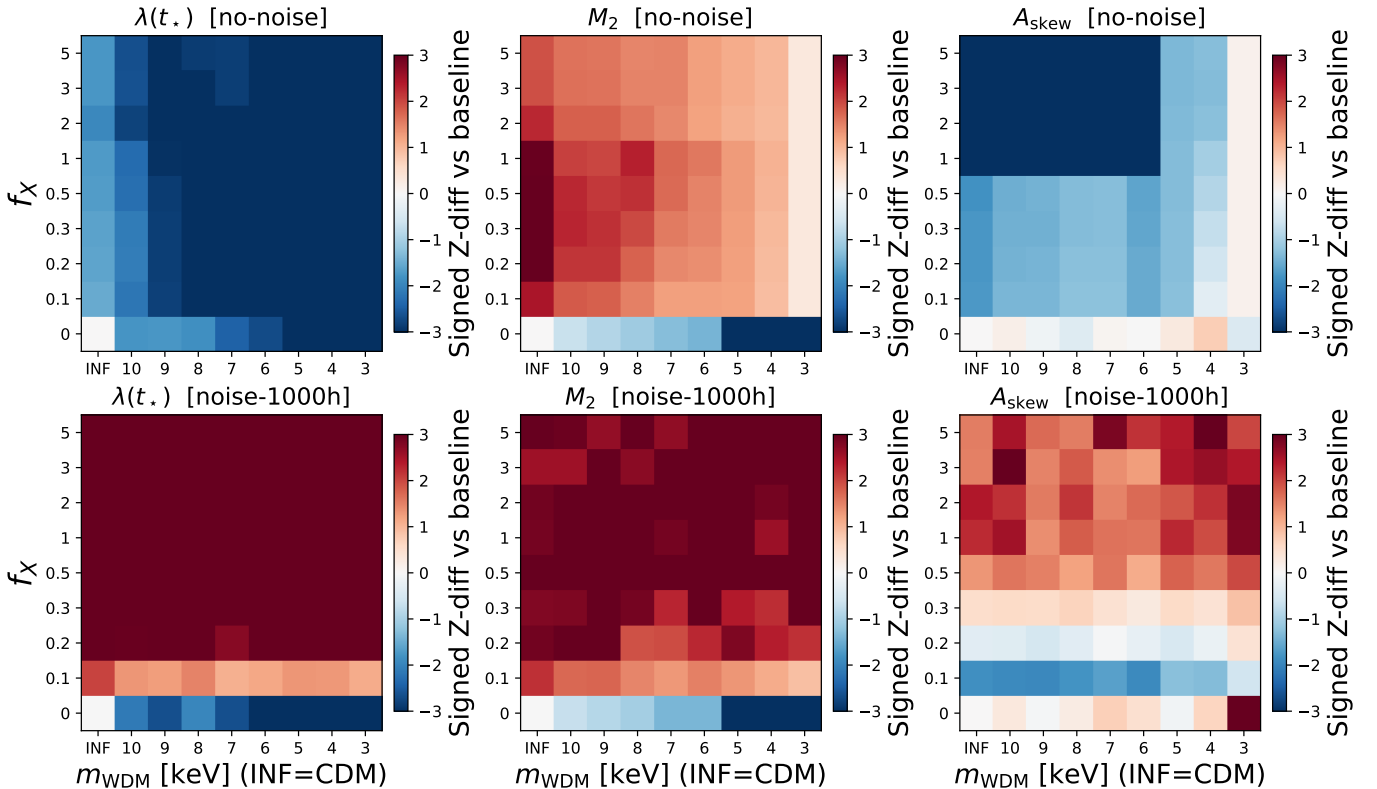


FIG. 7: Topological descriptor maps across (f_X, m_{WDM}) , shown as signed differences relative to the baseline CDM model ($f_X = 0$). Columns show $\lambda(t_*)$, M_2 , and A_{skew} . The top row is noiseless and the bottom row includes SKA1-Low thermal noise with $t_{\text{int}} = 1000$ h. Persistence-based quantities are computed using a common lifetime cut $\tau \geq \tau_*$.

matter physics in the presence of thermal noise.

V. SUMMARY & DISCUSSION

The topology of the 21 cm forest provides complementary information about the thermal and structural state of the intergalactic medium that is not captured by traditional amplitude-based statistics. The three topological descriptors introduced in this work—the trough line density $\lambda(t_*)$, the total squared persistence M_2 , and the Betti-curve asymmetry A_{skew} —probe distinct physical aspects of absorption morphology and therefore respond to heating and dark-matter free-streaming in fundamentally different ways.

A. Persistence-based topology as a non-Gaussian probe

It is also interesting to connect our persistence-based approach to other non-Gaussian statistics that have been widely used for the 21 cm brightness-temperature field. In particular, the bispectrum (i.e., the Fourier-space three-point function) is sensitive to phase correlations

and nonlinear mode coupling, while Minkowski functionals quantify excursion-set morphology in real space[e.g. 37–48]. These ideas can be adapted to the 21 cm forest as well, but with a practically important caveat: forest observables are line-like absorption features on top of a source-dependent continuum, so preprocessing choices (e.g., detrending, windowing, masking, and normalization) can more directly impact bispectrum- or amplitude-based morphology measures. In this respect, persistence summaries provide a complementary viewpoint because they emphasize the birth–merger hierarchy of troughs under sublevel filtrations and naturally down-weight short-lived, noise-induced structures through persistence filtering. A systematic comparison, and ultimately a joint analysis, of persistence descriptors with bispectrum/Minkowski-type summaries may therefore help clarify which aspects of non-Gaussianity are uniquely captured by topology and how robust each family of statistics is under realistic bandpass and continuum uncertainties.

B. Physical interpretation of the three descriptors

The line density $\lambda(t_*)$ traces the abundance of independent absorption troughs above a fixed persistence cut.

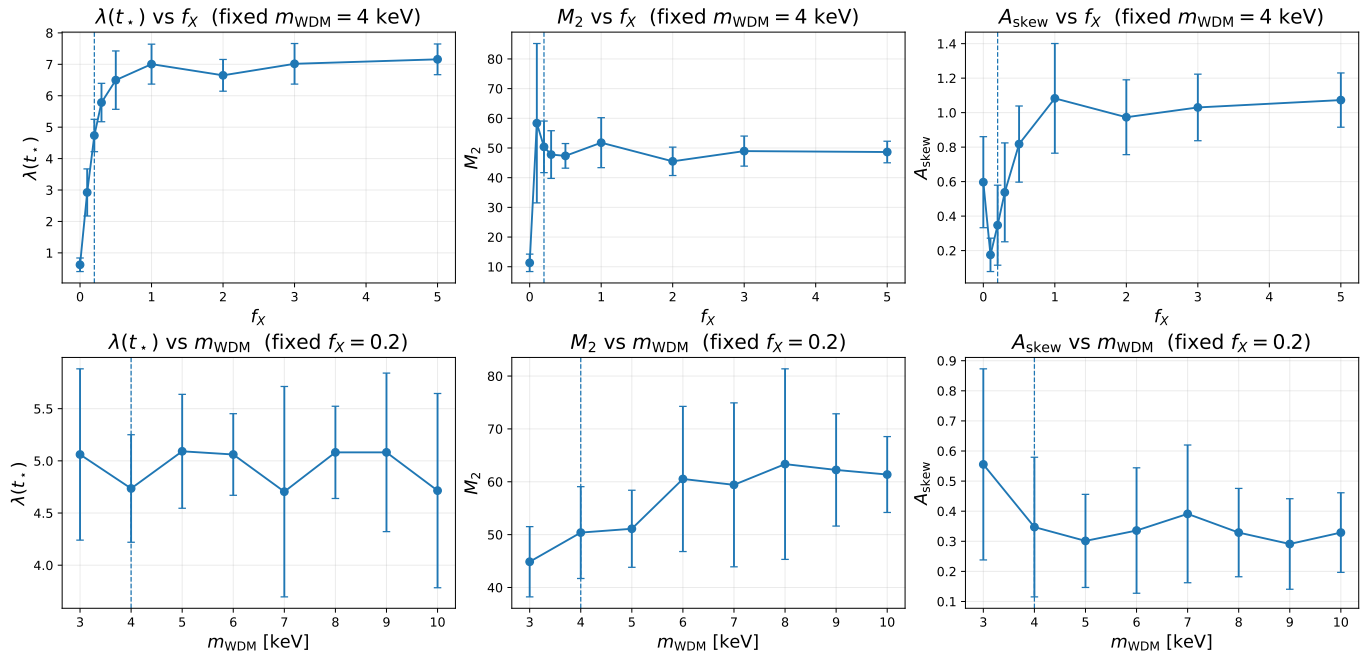


FIG. 8: Slice (intercept) plots through the fiducial model for the 1000 h noise branch. Top row: metric versus f_X at fixed $m_{\text{WDM}} = 4$ keV. Bottom row: metric versus m_{WDM} at fixed $f_X = 0.2$. The dashed line marks the fiducial value on each axis. These trends explain the orientations of the single-metric degeneracy directions in Figure 9: $\lambda(t_*)$ and A_{skew} are locally most sensitive to f_X , while M_2 retains sensitivity to both f_X and m_{WDM} .

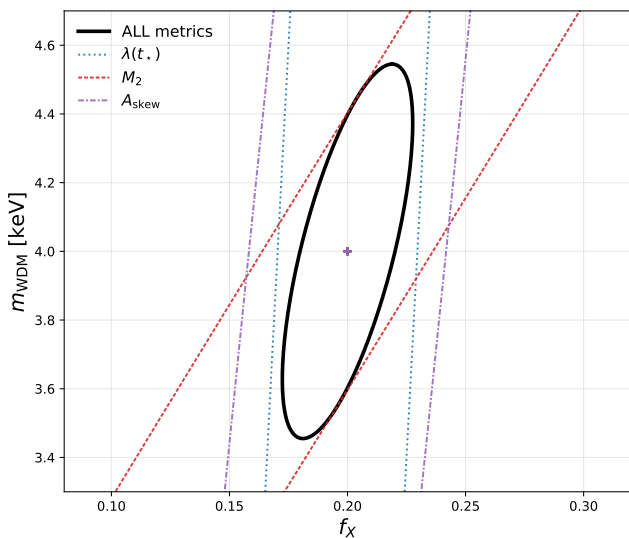


FIG. 9: Fisher-matrix forecast for the joint constraints on f_X and m_{WDM} using SKA1-Low-like thermal noise with 1000 h integration. The black contour shows the combined 1σ constraint from $\{\lambda(t_*), M_2, A_{\text{skew}}\}$ evaluated at the fiducial point $(f_X, m_{\text{WDM}}) = (0.2, 4 \text{ keV})$ (cross). Colored contours show the single-metric constraints, which are highly elongated because a single observable yields a Fisher matrix close to rank one in a two-parameter space.

In principle, warm dark matter erases small-scale density fluctuations and removes shallow extrema, which can re-

duce the number of identifiable troughs. However, once realistic SKA1-Low thermal noise is included and short-lived features are filtered out, the dominant variation of $\lambda(t_*)$ in the fiducial neighborhood is driven by the heating parameter. In particular, around $(f_X, m_{\text{WDM}}) = (0.2, 4 \text{ keV})$ the slice trends show a strong change of $\lambda(t_*)$ with f_X but a comparatively mild dependence on m_{WDM} , implying that $\lambda(t_*)$ primarily constrains f_X locally and yields a nearly vertical single-metric degeneracy direction in the Fisher plane (see Figs. 8 and 9). This emphasizes that Fisher orientations are controlled by the *local* gradients at the fiducial point rather than by global monotonic trends across the full grid.

The statistic M_2 measures the cumulative strength of long-lived absorption features through the total squared persistence, $M_2 = \sum_{j \in I_{\text{long}}} \tau_j^2$. Both warm dark matter and X-ray heating can reduce M_2 , but through qualitatively different modifications of the persistence hierarchy. Warm dark matter suppresses small-scale structure, removes shallow minima, and accelerates mergers between neighboring troughs, thereby shifting the lifetime distribution toward smaller τ and depleting its long- τ tail. X-ray heating, in contrast, primarily compresses the contrast of surviving features, shortening their persistence without necessarily eliminating the underlying rank ordering. Because M_2 weights lifetimes quadratically, it is particularly sensitive to the suppression of the long- τ tail and therefore retains appreciable sensitivity to m_{WDM} even in the presence of noise and persistence filtering. As a result, M_2 typically follows a moderately inclined

degeneracy direction, placing it between $\lambda(t_*)$ and A_{skew} in terms of parameter response.

The Betti-curve asymmetry A_{skew} encodes the relative support of $\beta_0(t)$ on the deep and shallow sides of the distribution. In our models, X-ray heating distorts this balance by shifting absorption toward shallower thresholds and broadening the shallow wing of $\beta_0(t)$. Warm dark matter primarily changes the abundance of small-scale structure and the overall number of components, while producing a weaker change in the deep–shallow imbalance of the surviving Betti support. As a result, A_{skew} is primarily sensitive to the heating efficiency f_X and only weakly dependent on m_{WDM} over the parameter range explored here, yielding a degeneracy direction that is nearly vertical.

C. Degeneracy breaking in the Fisher forecast

Because $\lambda(t_*)$ and A_{skew} both carry strong local sensitivity to f_X in the fiducial neighborhood, degeneracy breaking does not arise simply from an orthogonality between these two metrics alone. Instead, the key complementarity is that M_2 retains appreciable sensitivity to m_{WDM} (and to f_X), supplying the inclined direction needed to reduce the remaining degeneracy when the three metrics are combined. In other words, in the noise-included forecast relevant for SKA1-Low, the role of the three metrics is naturally interpreted as: $\lambda(t_*)$ and A_{skew} primarily anchor the heating axis, while M_2 provides the additional leverage on the free-streaming scale needed for a joint constraint.

We also note that the dominant topological transition associated with heating often occurs between the strictly unheated case ($f_X = 0$) and models with $f_X > 0$, while further increases in f_X produce more incremental changes. This threshold-like behavior is consistent with the rapid contrast compression once heating is present, and it explains why the local Fisher sensitivity to f_X can be large even when global trends appear to saturate at high heating.

D. Local versus global trends

When combined in a Fisher analysis, the complementary sensitivity directions of $\{\lambda(t_*), M_2, A_{\text{skew}}\}$ yield substantially tighter constraints on (f_X, m_{WDM}) than any individual statistic alone. The black confidence ellipse in Fig. 9 illustrates this effect. It is important, however, to distinguish between (i) a statistic showing a large dynamic range across the full (f_X, m_{WDM}) grid and (ii) its ability to break parameter degeneracies in a local Gaussian forecast. The Fisher orientation and constraining power are controlled by the local gradients evaluated at the fiducial point, not by global monotonic trends over the entire plane. In the noise-included case this distinction becomes especially relevant: thermal noise intro-

duces many short-lived, shallow fluctuations that are removed by the persistence cut, so the remaining long-lived topology is governed by a restricted subset of structures whose local response can differ from the global trend. Consequently, a descriptor may vary strongly across the plane yet still produce a highly elongated single-metric ellipse if its local response aligns with a single direction in (f_X, m_{WDM}) .

In our forecast near $(f_X, m_{\text{WDM}}) = (0.2, 4 \text{ keV})$, $\lambda(t_*)$ and A_{skew} provide strong local leverage on the heating axis, while M_2 retains appreciable sensitivity to m_{WDM} (and to f_X), supplying an inclined constraint direction with non-negligible free-streaming dependence. Their combination therefore reduces the allowed parameter volume substantially compared to any individual statistic, demonstrating that persistence-based descriptors of the 21 cm forest contain information that is complementary to and qualitatively distinct from amplitude-based summaries.

E. Robustness to thermal noise

Thermal noise predominantly introduces short-lived fluctuations, which are removed by applying a uniform persistence cut and therefore do not dominate the long-lived components that determine $\lambda(t_*)$, M_2 , and A_{skew} . As a result, the qualitative slice trends and the principal Fisher degeneracy directions remain stable under the uncorrelated thermal-noise model considered here, although the overall constraining power depends on the available number of independent background sources and on the noise level.

F. Caveats and future extensions

Several observational and physical effects not fully explored here will be important when applying these descriptors to real data, and we briefly comment on their expected impact.

First, while ~ 20 radio-loud sources may exist at $z \simeq 9$, an initial detection of the 21 cm forest will likely rely on a single spectrum. In this regime, a dominant limitation can be sample variance rather than thermal noise once a sufficient S/N is reached: $\lambda(t_*)$, M_2 , and A_{skew} fluctuate across lines of sight because the number and clustering of absorption troughs are set by rare overdense structures. Our Fisher forecast assumes N_{los} independent background sources; in the idealized limit of independent sightlines, the measurement uncertainties of the summary statistics decrease approximately as $1/\sqrt{N_{\text{los}}}$, and the resulting parameter constraints typically improve in a similar manner. For $N_{\text{los}} = 1$, meaningful constraints may still be achievable in favorable cases, such as exceptionally bright background sources observed with long integration times, but the inference becomes sensitive to cosmic variance and prior assumptions. For early data, a

practical use of the topological descriptors is therefore model discrimination (e.g., excluding extreme heating scenarios or very warm dark-matter models) rather than precision parameter estimation. We also emphasize that our Fisher estimate adopts a diagonal covariance between the three metrics; estimating the full cross-covariance will require substantially larger simulation ensembles and is left for future work. Finally, quantifying the stability of the Betti curves and persistence-based descriptors under LOS resampling (e.g., bootstrap/jackknife) will require larger simulated ensembles and is left for future work.

Second, the present analysis targets Cosmic Dawn, where the forest forms in a largely neutral intergalactic medium and its morphology is shaped primarily by heating and small-scale structure. At lower redshifts ($z \lesssim 7$), where radio-loud quasars have already been identified, inhomogeneous reionization introduces ionized bubbles and partially ionized regions that truncate absorption segments and modify the merger hierarchy encoded in $\beta_0(t)$. In this regime, the descriptors may become simultaneously sensitive to ionization topology and temperature, and an interpretation in terms of (f_X, m_{WDM}) alone will require (at least) additional parameters or external constraints, such as independent estimates of the global neutral fraction or characteristic bubble sizes. Nevertheless, the topological framework itself remains applicable: ionized gaps and bubble boundaries generate connectivity-driven signatures that can be captured by the same persistence formalism, suggesting a natural extension to joint inference of heating, small-scale structure, and reionization morphology.

Third, peculiar velocities enter the optical depth through the line-of-sight velocity-gradient term and can both enhance absorption amplitudes and alter the apparent clustering of features in frequency space. Because our analysis standardizes each spectrum and emphasizes rank ordering and connectivity, purely multiplicative amplitude boosts are expected to have a limited impact. However, velocity-induced reordering of shallow extrema or shifts in the relative separations of neighboring troughs can affect $\lambda(t_*)$ and the population of short-lived components. A quantitative assessment including full redshift-space distortions is therefore an important next step, particularly to test whether the nearly orthogonal responses of $\{\lambda(t_*), M_2, A_{\text{skew}}\}$ persist when velocity effects are modeled self-consistently.

Finally, in realistic observations the thermal-noise level depends on the flux density and intrinsic spectral shape of the background radio source, as well as on the channel width $\Delta\nu$ through the radiometer equation. In this work, spectral resolution and integration time were varied separately to isolate their qualitative effects on topology. A fully consistent forward model would vary the noise amplitude together with $\Delta\nu$ and marginalize over uncertainties in the background continuum, calibration residuals, and bandpass structure, as well as possible frequency correlations in the noise. While such refinements can shift the absolute performance forecasts, the central

trends reported here are driven by long-lived troughs and the gross shape of $\beta_0(t)$, which are comparatively stable once short-lived components are removed.

Because noise-induced features are preferentially short-lived, persistence filtering provides a natural mitigation. In practice, the optimal choice of τ_* and the associated information loss should be calibrated under realistic observing conditions; however, varying τ_* within a reasonable range does not change the qualitative parameter responses of $\{\lambda(t_*), M_2, A_{\text{skew}}\}$ in our simulations.

VI. CONCLUSION

We have shown that persistence-based topology provides a physically interpretable and complementary analysis layer for the 21 cm forest, helping to disentangle X-ray heating from dark-matter free-streaming. By tracking the birth–merger hierarchy of absorption troughs through sublevel filtrations of detrended, standardized one-dimensional forest spectra, we construct persistence diagrams and Betti-0 curves that encode connectivity and ordering information beyond two-point statistics.

From these topological summaries we defined three descriptors with clear interpretations: the trough line density $\lambda(t_*)$, the total squared persistence M_2 , and the Betti-curve asymmetry A_{skew} . In our SKA1-Low noise-included forecasts, $\lambda(t_*)$ and A_{skew} provide strong local leverage on the heating axis, while M_2 retains appreciable sensitivity to the free-streaming scale and supplies the additional constraint direction needed to reduce the remaining degeneracy. More generally, the relative sensitivity of each descriptor can vary across the parameter plane because Fisher information is governed by local gradients; the key result is that the three descriptors probe distinct aspects of the merger hierarchy and Betti support and therefore provide non-redundant information when combined.

The same persistence-based framework is readily applicable to other one-dimensional absorption fields such as the Ly α forest, offering a unified route to non-Gaussian inference that emphasizes connectivity and merger hierarchy. Applied to high-quality data from next-generation facilities such as the SKA, these topology-based descriptors provide a geometry-aware window on early structure formation and the microphysics of dark matter, naturally complementing power-spectrum and wavelet-based analyses.

Acknowledgments

This work is supported by the National SKA Program of China (No.2020SKA0110401), NSFC (Grant No. 12103044), and Yunnan Provincial Key Laboratory of Survey Science with project No. 202449CE340002.

-
- [1] C. L. Carilli, N. Y. Gnedin, and F. Owen, *ApJ* **577**, 22 (2002), astro-ph/0205169.
- [2] S. R. Furlanetto and A. Loeb, *ApJ* **579**, 1 (2002), astro-ph/0206308.
- [3] S. R. Furlanetto, *MNRAS* **370**, 1867 (2006), ISSN 0035-8711.
- [4] B. Ciardi, P. Labropoulos, A. Maselli, R. Thomas, S. Zaroubi, L. Graziani, J. S. Bolton, G. Bernardi, M. Brentjens, A. G. de Bruyn, et al., *MNRAS* **428**, 1755 (2013), 1209.2615.
- [5] B. Ciardi, S. Inoue, K. Mack, Y. Xu, and G. Bernardi, in *Advancing Astrophysics with the Square Kilometre Array (AASKA14)* (2015), p. 6, 1501.04425.
- [6] Y. Xu, X. Chen, Z. Fan, H. Trac, and R. Cen, *ApJ* **704**, 1396 (2009), 0904.4254.
- [7] Y. Xu, A. Ferrara, and X. Chen, *MNRAS* **410**, 2025 (2011), 1009.1149.
- [8] H. Shimabukuro, K. Ichiki, S. Inoue, and S. Yokoyama, *Phys. Rev. D* **90**, 083003 (2014), 1403.1605.
- [9] B. Semelin, *MNRAS* **455**, 962 (2016), 1510.02296.
- [10] H. Shimabukuro, K. Ichiki, and K. Kadota, *Phys. Rev. D* **101**, 043516 (2020), 1910.06011.
- [11] H. Shimabukuro, K. Ichiki, and K. Kadota, *Phys. Rev. D* **102**, 023522 (2020), 2005.05589.
- [12] T. Šoltinský, J. S. Bolton, N. Hatch, M. G. Haehnelt, L. C. Keating, G. Kulkarni, E. Puchwein, J. Chardin, and D. Aubert, *MNRAS* **506**, 5818 (2021), 2105.02250.
- [13] M. Kawasaki, W. Nakano, H. Nakatsuka, and E. Sonomoto, *J. Cosmology Astropart. Phys.* **2021**, 019 (2021), 2010.13504.
- [14] H. Shimabukuro, K. Ichiki, and K. Kadota, *Phys. Rev. D* **107**, 123520 (2023), 2212.08409.
- [15] P. Villanueva-Domingo and K. Ichiki, *PASJ* **75**, S33 (2023), 2104.10695.
- [16] Y. Shao, T.-Y. Sun, M.-L. Zhao, and X. Zhang, *Phys. Rev. D* **112**, 063513 (2025), 2411.17094.
- [17] H. Shimabukuro, S. Liu, and B. Li, arXiv e-prints arXiv:2512.00402 (2025), 2512.00402.
- [18] N. Thyagarajan, *ApJ* **899**, 16 (2020), 2006.10070.
- [19] Y. Shao, Y. Xu, Y. Wang, W. Yang, R. Li, X. Zhang, and X. Chen, *Nature Astronomy* **7**, 1116 (2023), 2307.04130.
- [20] T. Šoltinský, G. Kulkarni, S. P. Tendulkar, and J. S. Bolton, *MNRAS* **537**, 364 (2025).
- [21] H. M. Tohfa, S. Bird, M.-F. Ho, M. Qezlou, and M. Fernandez, *Phys. Rev. Lett.* **132**, 231002 (2024), 2310.06010.
- [22] H. Shimabukuro, Y. Xu, and Y. Shao, *Phys. Rev. D* **112**, 063557 (2025), 2504.14656.
- [23] T.-Y. Sun, Y. Shao, Y. Li, Y. Xu, H. Wang, and X. Zhang, *Communications Physics* **8**, 220 (2025), 2407.14298.
- [24] S. K. Patil, T. Šoltinský, S. Maitra, and G. Kulkarni, arXiv e-prints arXiv:2507.11611 (2025), 2507.11611.
- [25] N. Otter, M. A. Porter, U. Tillmann, P. Grindrod, and H. A. Harrington, arXiv e-prints arXiv:1506.08903 (2015), 1506.08903.
- [26] L. Wasserman, arXiv e-prints arXiv:1609.08227 (2016), 1609.08227.
- [27] S. Gholizadeh and W. Zdrozny, arXiv e-prints arXiv:1809.10745 (2018), 1809.10745.
- [28] P. Pranav, H. Edelsbrunner, R. van de Weygaert, G. Vegter, M. Kerber, B. J. T. Jones, and M. Wintraecken, *MNRAS* **465**, 4281 (2017), 1608.04519.
- [29] W. Elbers and R. van de Weygaert, *MNRAS* **486**, 1523 (2019), 1812.00462.
- [30] G. Wilding, K. Nevenzeel, R. van de Weygaert, G. Vegter, P. Pranav, B. J. T. Jones, K. Efstathiou, and J. Feldbrugge, *MNRAS* **507**, 2968 (2021), 2011.12851.
- [31] S. Heydenreich, B. Brück, and J. Harnois-Déraps, *A&A* **648**, A74 (2021), 2007.13724.
- [32] W. Elbers and R. van de Weygaert, *MNRAS* **520**, 2709 (2023), 2209.03948.
- [33] R. Bermejo, G. Wilding, R. van de Weygaert, B. J. T. Jones, G. Vegter, and K. Efstathiou, *MNRAS* **529**, 4325 (2024), 2206.14655.
- [34] J. Calles, J. H. T. Yip, G. Contardo, J. Noreña, A. Rouhinen, and G. Shiu, *J. Cosmology Astropart. Phys.* **2025**, 064 (2025), 2412.15405.
- [35] R. Braun, A. Bonaldi, T. Bourke, E. Keane, and J. Wagg, *Anticipated performance of the square kilometre array – phase 1 (ska1)* (2019), 1912.12699, URL <https://arxiv.org/abs/1912.12699>.
- [36] Q. Niu, Y. Li, Y. Xu, H. Guo, and X. Zhang, *ApJ* **978**, 145 (2025), 2407.18136.
- [37] C. A. Watkinson, S. Majumdar, J. R. Pritchard, and R. Mondal, *MNRAS* **472**, 2436 (2017), 1705.06284.
- [38] S. Majumdar, J. R. Pritchard, R. Mondal, C. A. Watkinson, S. Bharadwaj, and G. Mellema, *MNRAS* **476**, 4007 (2018), 1708.08458.
- [39] H. Shimabukuro, S. Yoshiura, K. Takahashi, S. Yokoyama, and K. Ichiki, *MNRAS* **458**, 3003 (2016), 1507.01335.
- [40] H. Shimabukuro, S. Yoshiura, K. Takahashi, S. Yokoyama, and K. Ichiki, *MNRAS* **468**, 1542 (2017), 1608.00372.
- [41] S. Yoshiura, H. Shimabukuro, K. Takahashi, and T. Matsumura, *MNRAS* **465**, 394 (2017), 1602.02351.
- [42] S. Bag, R. Mondal, P. Sarkar, S. Bharadwaj, and V. Sahni, *MNRAS* **477**, 1984 (2018), 1801.01116.
- [43] A. Kapahtia, P. Chingangbam, S. Appleby, and C. Park, *J. Cosmology Astropart. Phys.* **2018**, 011 (2018), 1712.09195.
- [44] Z. Chen, Y. Xu, Y. Wang, and X. Chen, *ApJ* **885**, 23 (2019), 1812.10333.
- [45] A. Kapahtia, P. Chingangbam, and S. Appleby, *J. Cosmology Astropart. Phys.* **2019**, 053 (2019), 1904.06840.
- [46] A. Kapahtia, P. Chingangbam, R. Ghara, S. Appleby, and T. R. Choudhury, *J. Cosmology Astropart. Phys.* **2021**, 026 (2021), 2101.03962.
- [47] S. K. Giri and G. Mellema, *MNRAS* **505**, 1863 (2021), 2012.12908.
- [48] B. Spina, C. Porciani, and C. Schimd, *MNRAS* **505**, 3492 (2021), 2101.09288.